ADVANCED FUNCTIONAL MATERIALS
www.afm-journal.de

Photochemical Deposition of Highly Dispersed Pt Nanoparticles on Porous CeO_2 Nanofibers for the Water-Gas Shift Reaction

*Ping Lu, Botao Qiao, Ning Lu, Dong Choon Hyun, Jinguo Wang, Moon J. Kim, Jingyue Liu, and Younan Xia**

Ceria (CeO_2) nanofibers with high porosity are fabricated using an approach involving sol–gel, electrospinning, and calcination. Specifically, cerium(III) acetylacetonate and polyacrylonitrile (PAN) are dissolved in *N*,*N*-dimethylformamide (DMF) and then electrospun into nanofibers. The PAN matrix plays a critical role in stabilizing the porous structure from collapse during calcination in air up to 800 °C. CeO_2 porous nanofibers comprising an interconnected network of single crystalline and fully oxidized CeO_2 nanoparticles about 40 nm in size are obtained. The hierarchically porous structure of the CeO_2 nanofibers enables the facile deposition of Pt nanoparticles via heterogeneous nucleation in a photochemical method. When conducted in the presence of poly(vinyl pyrrolidone) (PVP) and 4-benzyolbenzoic acid, uniform Pt nanoparticles with an average diameter of 1.7 nm are obtained, which are evenly dispersed across the entire surface of each CeO_2 nanofiber. The high porosity of CeO_2 nanofibers and the uniform distribution of Pt nanoparticles greatly improve the activity and stability of this catalytic system toward the water-gas shift reaction. It is believed that this method could be extended to produce a variety of catalysts and systems sought for various industrial applications.

1. Introduction

Ceria (CeO_2) has attracted intense and widespread interest in recent years due to its unique properties.[1] For example, CeO_2 is capable of switching easily and rapidly between Ce^{3+} and Ce^{4+} under alternating oxidizing and reducing environments.[2] This characteristic makes it an excellent oxygen buffer for the balance of oxygen level in a reaction system by automatically storing and releasing oxygen. Furthermore, CeO_2 has high thermal and chemical stability, in addition to a wide band gap, large dielectric constant, and high ionic conductivity. As a result, CeO_2-based nanomaterials have been extensively explored as catalysts and catalytic supports or promoters for automobile exhaust conversion, electrolytes for solid oxide fuel cells (SOFCs), abrasive materials for chemical–mechanical planarization, gas sensors, ultraviolet absorbents, and cosmetic materials.[3] Motivated by the fascinating properties and the promising applications, a lot of efforts have recently been directed toward the controlled synthesis or fabrication of CeO_2 nanostructures.[4]

1D nanostructures have been the subject of considerable research due to their large surface area, high porosity, high aspect ratio, and superior mechanical flexibility.[5] Among the various techniques capable of generating 1D nanostructures, electrospinning represents a simple, convenient, and versatile method for the fabrication of nanofibers. Most importantly, electrospinning is the only available technique capable of producing continuous nanofibers of polymers, metals, and oxides from a variety of polymers and precursors in large quantities for catalytic applications.[6] However, the fabrication of high-quality CeO_2 nanofibers is extremely difficult because of the peculiar characteristics of the Ce-containing salts or organometallic precursors. Shao et al. reported the preparation of CeO_2 nanofibers by electrospinning an aqueous solution of $Ce(NO_3)_3$ and poly(vinyl alcohol) (PVA), followed by calcination of the $Ce(NO_3)_3$-PVA composite fibers.[7] In the electrospinning, the authors used gravity to control the solution flow, which led to unstable and unsustainable polymer feeding and thus the formation of nanofibers with irregular diameters. They did not disclose the parameters for the electrospinning neither, making the reproduction of their work difficult. In a separate study, Lei and co-workers produced CeO_2 nanofibers using poly(vinyl

Dr. P. Lu, Dr. D. C. Hyun, Prof. Y. Xia
The Wallace H. Coulter Department of
Biomedical Engineering
Georgia Institute of Technology
and Emory University
Atlanta, GA 30332, USA
E-mail: younan.xia@bme.gatech.edu

Dr. B. Qiao, Prof. J. Liu
Department of Physics
Arizona State University
Tempe, AZ 85287, USA

Dr. N. Lu, Dr. J. Wang, Prof. M. J. Kim
Department of Materials Science and Engineering
University of Texas at Dallas
Richardson, TX 75080, USA

Prof. Y. Xia
School of Chemistry and Biochemistry
School of Chemical and Biomolecular Engineering
Georgia Institute of Technology
Atlanta, GA 30332, USA

DOI: 10.1002/adfm.201501392

pyrrolidone) (PVP) as the polymer matrix and $Ce(NO_3)_3$ as the precursor.[3d] However, Alves et al. found that the $Ce(NO_3)_3$-based composite fibers could not maintain their morphology during calcination and the fibers collapsed to evolve into a monolith.[8] They speculated that the deformation was caused by the energetic decomposition of nitrates under thermal treatment. In addition to pure CeO_2 nanofibers, many efforts have been made toward the fabrication of oxide-doped CeO_2 nanofibers. For example, Azad et al. prepared Gd_2O_3-doped CeO_2 nanofibers by electrospinning an solution containing $(NH_4)_2Ce(NO_3)_6$, $Gd(NO_3)_3$, and PVP.[9] Cao and co-workers produced CeO_2–ZrO_2 nanofibers by electrospinning an alcohol solution containing $Ce(NO_3)_3$, $ZrOCl_2$, and PVP.[10] Song et al. fabricated In_2O_3–CeO_2 nanotubes by electrospinning a *N,N*-dimethylformamide (DMF) solution containing $In(NO_3)_3$, $Ce(NO_3)_3$, and PVP, followed by a heating treatment.[11] Although these methods were able to produce a small amount of CeO_2 or CeO_2-containing nanofibers, we still lack an effective method for the production of high-quality CeO_2 nanofibers in terms of controls for the size, uniformity, porosity, and yield.

We noticed that the electrospinning process was highly unstable when we tried to use the polymers, precursor salts, and parameters reported in the literature. The ejection of liquid jet was frequently stopped by solution dripping and clogging, resulting in the formation of low-quality samples with droplets and irregular fibers (Figure S1a–d, Supporting Information). Furthermore, the generated CeO_2 nanofibers were nonporous and fused together to form large pieces after calcination, which was similar to what was observed in the previous studies.[8,10,12] The low quality and low yield of CeO_2 nanofibers produced by electrospinning severely hinder their practical applications in catalysis. In order to solve this problem, a proper combination of polymer, precursor, solvent, and electrospinning parameters needs to be developed for the reliable production of CeO_2 nanofibers. Among various cerium salts tested, we found that cerium(III) acetylacetonate, $Ce(acac)_3$, could be an excellent candidate due to its compatibility with various polymers and solvents. However, it was observed that $Ce(acac)_3$ tended to melt and thus become mobile in the composite fibers during calcination, leading to the formation of irregular fibers.[8] Therefore, it is necessary to select a polymer that is capable of maintaining the fiber morphology and thus entrapping $Ce(acac)_3$ before it solidifies into inorganic phase during calcination. It is well-known that polyacrylonitrile (PAN) fibers are stable in air up to 600 °C in terms of physical morphology even though the chemical structure is converted to carbonaceous species.[13] On the other hand, $Ce(acac)_3$ can be transformed to the stable CeO_2 phase at 300–400 °C while the residue carbon can be readily removed by heating the composite nanofibers to higher temperatures in air.[14] As such, CeO_2 nanofibers with uniform morphology can be generated.

Electrospun CeO_2 nanofibers are attractive supports for catalysts owing to their high surface area, large porosity, high oxygen storage capacity, and the ability to form strong metal–support interactions. Three methods can be utilized to introduce the catalyst nanoparticles onto the surface of CeO_2 nanofibers. The most straightforward one is to load preformed nanoparticles onto the surface of CeO_2 nanofibers. The obvious advantage of this method is that both the catalyst nanoparticles and the CeO_2 nanofibers can be separately controlled and optimized. However, this method involves multiple steps and thus is time-consuming. Furthermore, preformed catalyst nanoparticles have strong tendency to form agglomerates on the supports, which can lead to significant sintering at elevated temperatures in practical applications.[15] The alternative is to impregnate the CeO_2 with a precursor solution to the catalyst nanoparticles. Under proper reducing conditions, nanoparticles can be generated on the surface and in the pores of the supports. This method is characterized by its simplicity and has been widely employed in industrial-scale catalytic applications. However, it is incapable of controlling the size and distribution of catalyst nanoparticles. Therefore, nanoparticles with polydispersity are typically obtained and poorly distributed across the surface of supports.[16] The third method is to take advantage of the fiber formation process in electrospinning to incorporate the catalyst nanoparticles.[17] Specifically, the catalyst precursors or preformed nanoparticles are mixed with the solution containing polymers and cerium salts and then the mixture are spun into composite fibers by electrospinning. Inorganic fibers containing CeO_2 and catalyst nanoparticles can be generated after the removal of organics and the conversion of precursors to oxides and metals under calcination and reduction. The strength of this method is that the catalyst nanoparticles are distributed homogeneously inside the fibers. But majority of the catalyst nanoparticles are embedded inside CeO_2, which are hardly accessible to the reactive species in catalysis. Additionally, the catalyst nanoparticles might have experienced more or less sintering during calcination treatment.[18] Furthermore, the addition of precursors can greatly affect the rheology and the conductivity of the polymer solution, resulting in the formation of low-quality nanofibers.[9]

Herein, we demonstrate a simple, three-step strategy combining electrospinning, calcination, and photochemical reduction for the synthesis of Pt/CeO_2 consisting of monodispersed Pt nanoparticles (~2 nm) and porous CeO_2 nanofibers. First, we developed an effective method for the large-scale production of porous CeO_2 nanofibers with large cavities by electrospinning and calcination. In the previous studies, only solid CeO_2 nanofibers were produced from a variety of polymer/precursor combinations by electrospinning.[3d,7–10],[12,17b,19] In this study, we chose PAN as the polymer matrix because of its ability in maintaining a stable fibrous structure up to 600 °C in air while most of the polymers used in previous studies decomposed below 300 °C.[3d,7],[8] As a result, the collapse of fibers and pores were effectively prevented and CeO_2 nanofibers with macropores were generated after the removal of carbon species by calcination in air at 800 °C. The hierarchical pore structure of nonwoven mat of CeO_2 nanofibers enabled in situ growth and deposition of metal nanoparticles via heterogeneous nucleation using photochemical method. Although it is known for a long time that CeO_2 can be utilized as UV absorbent,[3b] there is no report on the UV-assisted synthesis of Pt nanoparticles on the surface of CeO_2 through a photochemical route.[3h–3j] Our approach ensures not only the successful growth of monodispersed Pt nanoparticles on the porous CeO_2 nanofibers, but also the homogeneous dispersion of these nanoparticles across the entire surface without aggregation. The hierarchical porosity of CeO_2 nanofibers and the homogeneous distribution of monodispersed Pt nanoparticles improved the mass transfer of reactive species and the thermal stability of catalyst nanoparticles, leading to a much higher catalytic activity and stability in the water-gas shift reaction. To our knowledge, this work represents the first demonstration on the production of porous CeO_2 nanofibers with high quality and high reproducibility for practical applications. We believe that, by using this reproducible and cost-effective route, many other metal catalysts with controlled sizes and coverage densities could be deposited on the porous CeO_2 nanofibers for wide catalytic applications.

2. Results and Discussion

2.1. Fabrication of Porous CeO_2 Nanofibers

Composite nanofibers containing cerium was fabricated by electrospinning a solution containing $Ce(acac)_3$ (as a precursor to CeO_2), PAN (as a polymer carrier), and DMF (as a solvent). Both $Ce(acac)_3$ and PAN are readily soluble in DMF and demonstrated excellent compatibility by forming a clear brown solution. The spinning proceeded in a highly stable and reliable manner, producing a nonwoven mat of $Ce(acac)_3$-PAN composite nanofibers of 20 cm × 10 cm × 2 mm in dimensions within a few hours. Solution dripping and ejection of liquid droplets, which were common issues in previous studies that led to the formation of randomly large particles, were not observed within a period up to 3 h. As shown in Figure S1e (Supporting Information), the $Ce(acac)_3$-PAN composite nanofibers had a uniform diameter throughout the entire length and among different fibers. In addition, we did not observe any particles and irregular fibers by scanning across the entire samples (10 mm × 8 mm), which were cut from different regions of the nonwoven mat. This result confirms that the electrospinning of cerium-containing composite nanofibers was robust by switching to the current combination of polymer, precursor, solvent, and parameters. As such, we successfully solved the long-standing problem that prevented the fabrication of high-quality ceria precursory nanofibers in all previous studies.[9]

The second challenge in this study is to maintain the fibrous structure of the composite nanofibers during high-temperature calcination and then produce pure CeO_2 nanofibers. It was observed that $Ce(acac)_3$ could become a mobile phase under heating and completely lose the fiber structure if polymers with low decomposition temperature (e.g., PVP) were used as the matrix.[8] Since PAN can keep the fiber shape during the transformation to carbon phase under heating, it is expected that the collapse of $Ce(acac)_3$ in the process of converting to CeO_2 could be prevented. Indeed, the mat did not melt during calcination at 800 °C in air. The resultant CeO_2 nanofibers were then examined by scanning electron microscope (SEM) and transmission electron microscope (TEM), and the results are shown in **Figure 1**. It can be seen that the samples maintained the fibrous structure after the complete removal of PAN and the intermediate carbon species (Figure 1a). The sizes of the fibers before and after calcination were also measured, which showed a significant reduction after calcination. The $Ce(acac)_3$-PAN composite fibers had an average diameter of 740 nm (Figure S1f, Supporting Information) while the calcined nanofibers were only 169 nm (Figure 1b), corresponding to a shrinkage of 77% for the size. In spite of such a big size reduction, the calcined fibers still retained well-defined fiber morphology throughout the mat, demonstrating the homogeneous dispersion of CeO_2 precursor along the composite fibers. Unexpectedly, instead of forming solid fibers, the CeO_2 nanofibers contained a dense array of cavities and channels on their surface. The interconnected pores inside each nanofiber were generated probably due to the phase separation between $Ce(acac)_3$ and PAN, as well as the subsequent loss of PAN, the decomposition of $Ce(acac)_3$, and the crystallization of CeO_2.[13] More detailed morphology of the calcined nanofibers was investigated by TEM. Figure 1c shows a representative porous CeO_2 nanofiber and the small individual crystallites can be observed in the nanofibers. The high-angle annular dark-field scanning TEM (HAADF-STEM) image taken from the same nanofiber as shown in Figure 1d clearly reveals the porous structure with a sharp contrast. The porous CeO_2 nanofibers were made of interconnected nanoparticles with diameters in the range 10–90 nm (Figure S2, Supporting Information). Despite the attractive features of hierarchically porous CeO_2 nanomaterials, including high surface areas, short diffusion channels, and strong mechanical stability, porous CeO_2 nanofibers have not been reported in literature.[12] Our approach is the first of its kind to produce porous CeO_2 nanofibers of high quality in a reliable and controlled means.

The crystalline structure of porous CeO_2 nanofibers was investigated by different characterization techniques including selected area electron diffraction (SAED), powder X-ray diffraction (XRD), high-resolution TEM (HRTEM), and HAADF-STEM. The SAED of a nanofiber shows a typical ring pattern (**Figure 2**a), indicating that the porous CeO_2 nanofibers were polycrystalline. The composition and crystalline structure were further characterized by powder XRD. As shown in Figure 2b, the XRD pattern of porous CeO_2 nanofibers can be indexed to CeO_2 with a face-centered fluorite cubic structure (PDF 04-008-6546). The diffraction peaks at $2\theta = 28.8°$, 33.3°, 47.7°, 56.6°, 59.3°, 69.7°, 76.9°, and 79.3° could be designated to the (111), (200), (220), (311), (222), (400), (331), and (420) planes, respectively (Figure 2b). No other diffraction peaks were observed, suggesting the complete removal of PAN and carbon species as well as the good phase purity. Based on the (111) diffraction peak, the average crystalline size of CeO_2 was calculated to be around 40 nm using the Scherrer's equation, which is consistent with the TEM measurements (Figure S2, Supporting Information). Figure 2c shows the individual nanocrystals inside individual CeO_2 nanofibers. The interplanar spacings of 3.1 and 2.7 Å correspond to the (111) and (200) lattice planes of CeO_2, respectively. Figure 2d further confirms that each nanocrystal in the nanofiber was a piece of single crystal of CeO_2 with distinctive 2D lattice fringes. A large amount of single-crystal nanoparticles attached together to form a polycrystalline nanofiber with a hierarchical pore structure. The oxidation state of the calcined sample was investigated using X-ray photoelectron spectroscopy (XPS). Among the transition metal oxides, cerium oxide is characterized by its various oxidation states due to the hybridization of Ce 6s and 6p valence orbitals. Ce has two characteristic oxidation states which are +3 and +4.[3f,11],[20] **Figure 3**a shows the high-resolution XP spectra of Ce 3d region which

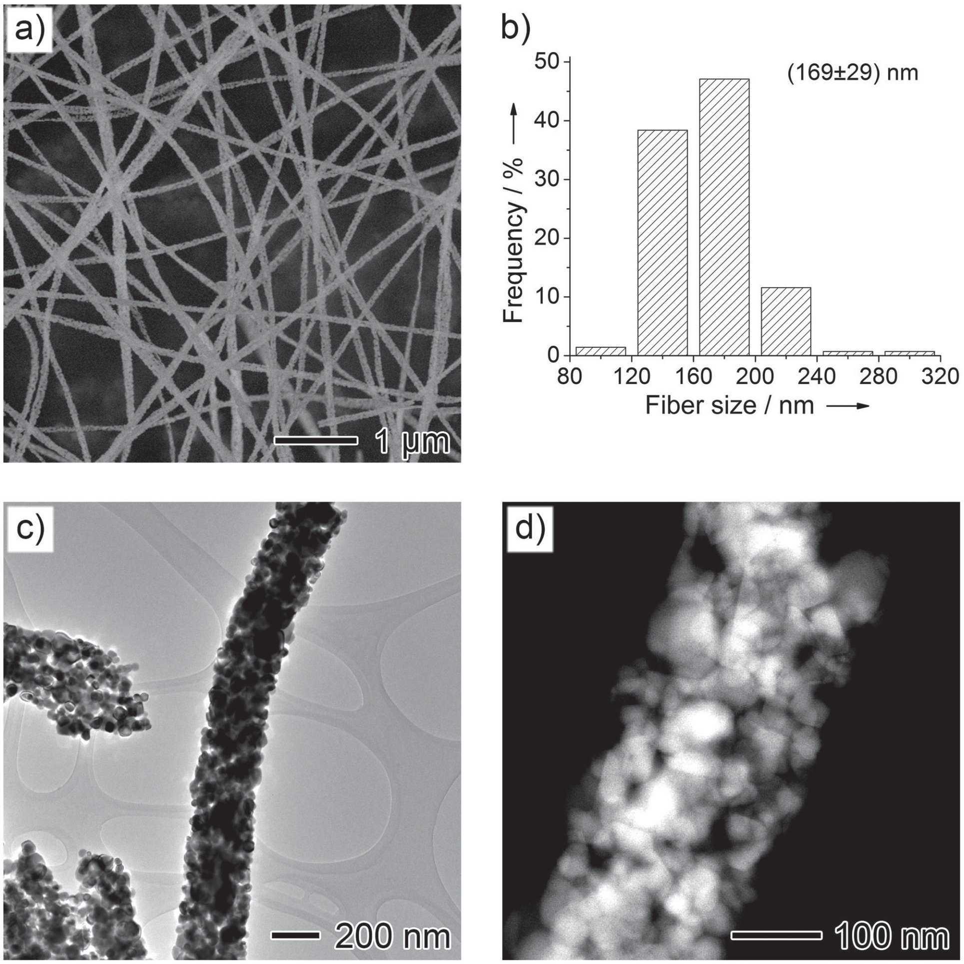

Figure 1. a) SEM image showing porous CeO_2 nanofibers prepared by calcination of the as-spun $Ce(acac)_3$-PAN composite nanofibers at 800 °C in air for 2 h and b) their size distribution. c) TEM and d) HAADF-STEM images showing the porous structure of a single CeO_2 nanofiber.

contains primarily Ce^{4+}, demonstrating that the calcination in air resulted in the complete oxidation of Ce.

2.2. Photochemical Synthesis and Deposition of Pt onto Porous CeO_2 Nanofibers

The porous CeO_2 nanofibers were employed as supports for the in situ synthesis and deposition of Pt nanoparticles using a photochemical route. In a typical process, the porous CeO_2 nanofibers were mixed with H_2PtCl_6 in a mixture of water and ethanol and then the dispersion was irradiated with UV light under cooling with circulating water. In our experiment, a 500 W quartz mercury vapor arc lamp was used as the light source with UV radiations in the range of 200–400 nm. The reduction of $PtCl_6^{2-}$ by ethanol under UV irradiation could be visually monitored using color changes to the solution: the precursor $PtCl_6^{2-}$ (Pt^{4+}) was yellow and the intermediate $PtCl_4^{2-}$ (Pt^{2+}) was orange, whereas Pt^0 was black. Harada and Einaga[21] found that the excited Pt^{4+} was first reduced by ethanol to Pt^{3+} upon UV irradiation. Subsequently, the oxidized ethanol molecules became highly reactive radicals, which reduced the Pt^{3+} to Pt^{2+} species. Additionally, the disproportionation of Pt^{3+} also generated Pt^{2+} species. The further reduction of Pt^{2+} species by ethanol under UV irradiation led to the formation of Pt^0 atoms, which aggregated to develop Pt nanoparticles through Pt^0-Pt^0 bond.[21] The product after washing and drying was dark gray, which was referred to as Pt_a/CeO_2. XRD was used to determine the crystallinity of the Pt nanoparticles. However, no Pt diffraction peak was observed in the XRD diffractogram (Figure S3, curve a, Supporting Information). The missing of Pt diffraction peaks is probably due to the low Pt loading (3%) and the small size of the Pt nanoparticles.[18] The presence of Pt on porous CeO_2 nanofibers was confirmed by XPS analysis. Figure 3b shows the Pt 4f core level spectrum, which includes only one set of 4f peaks. The Pt $4f_{5/2}$ and Pt $4f_{7/2}$ have binding energies at 75.0 and 71.7 eV, respectively, which are consistent with the literature values for bulk Pt.[4e] This result suggests that the Pt species on CeO_2 were completely reduced to Pt^0 during the UV irradiation in the presence of ethanol.

Figure 4a shows the HAADF-STEM image of Pt_a/CeO_2, in which large Pt agglomerates with sizes above 10 nm were observed. These Pt agglomerates contained a lot of Pt nanoparticles with an average diameter around 2–3 nm (Figure 4b). They had a rough surface and a porous structure, and were different from the CeO_2 nanoparticles in the porous fibers. The

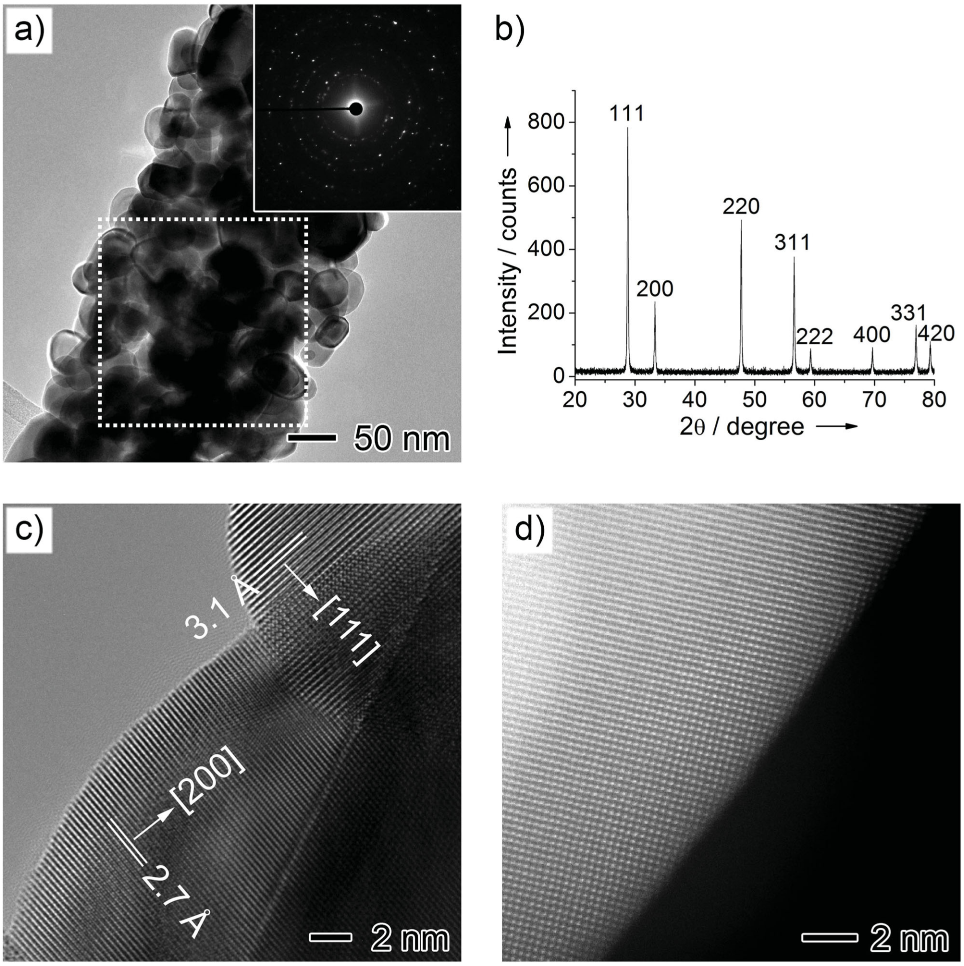

Figure 2. a) TEM image showing a single CeO_2 nanofiber and the corresponding SAED pattern (inset). b) XRD pattern of the CeO_2 nanofibers. c) HRTEM and d) HAADF-STEM images showing the single-crystal nanoparticles of CeO_2 contained in each nanofiber.

composition of these agglomerates was confirmed to be pure Pt using EDS. Figure 4c shows a representative agglomerate (Figure 4b, position 1) that only contained Pt while the underneath surface (Figure 4b, position 2) was made of Ce and O. The Cu signal came from the copper TEM grid, which was present in the spectra of both positions. The formation of Pt agglomerates was due to the lack of a colloidal stabilizer in the reaction medium. Because the naked Pt nanoparticles had a hydrophobic surface, they had a strong tendency to attach together in an effort to decrease the total surface area. In order to improve the dispersion of small Pt nanoparticles in water, we added PVP into the reaction solution as a colloidal stabilizer. Other parameters were kept the same as the previous process and the sample was referred to as Pt_b/CeO_2. As shown in Figure 4d–f, the introduction of PVP significantly decreased the size of the Pt nanoparticles and improved their dispersion on the surface of CeO_2 nanofibers. We did not observe large Pt agglomerates under TEM measurement. Figure 4d shows a representative Pt_b/CeO_2 sample, in which many small Pt nanoparticles were resolved on porous CeO_2 nanofibers. However, the distribution of Pt nanoparticles was not uniform across the surface of CeO_2. The Pt nanoparticles were crowded at some locations such as the interparticle pockets or pores (Figure 4e). They interacted with each other to form dimers, trimers, and small agglomerates, which could lead to significant sintering at elevated temperatures due to the short distance between these nanoparticles.[15b] This problem could not be solved by simply increasing the amount of PVP in the reaction solution.

In order to improve the dispersion of Pt nanoparticles on CeO_2, we introduced a UV-sensitive molecule, 4-benzyolbenzoic acid into the reaction solution. Under UV irradiation, 4-benzyolbenzoic acid is first excited to the singlet state and then transformed to triplet state with a lower energy level through intersystem crossing. The electronically excited 4-benzyolbenzoic acid molecule can abstract hydrogen from ethanol, which serves as a hydrogen donor, to generate the highly reactive ketyl radical species. These ketyl radicals are able to reduce Pt^{4+} to Pt^0, which then nucleate and grow into Pt nanoparticles.[22] This process is much faster than the direct photoreduction of Pt^{4+} to Pt^0 nanoparticles via the intermediate Pt^{2+} species.[23] As a result, the Pt nanoparticles generated in the presence of 4-benzyolbenzoic acid exhibited a distinctly smaller size as compared to those of the previous products. We could hardly differentiate Pt nanoparticles from the surface of porous

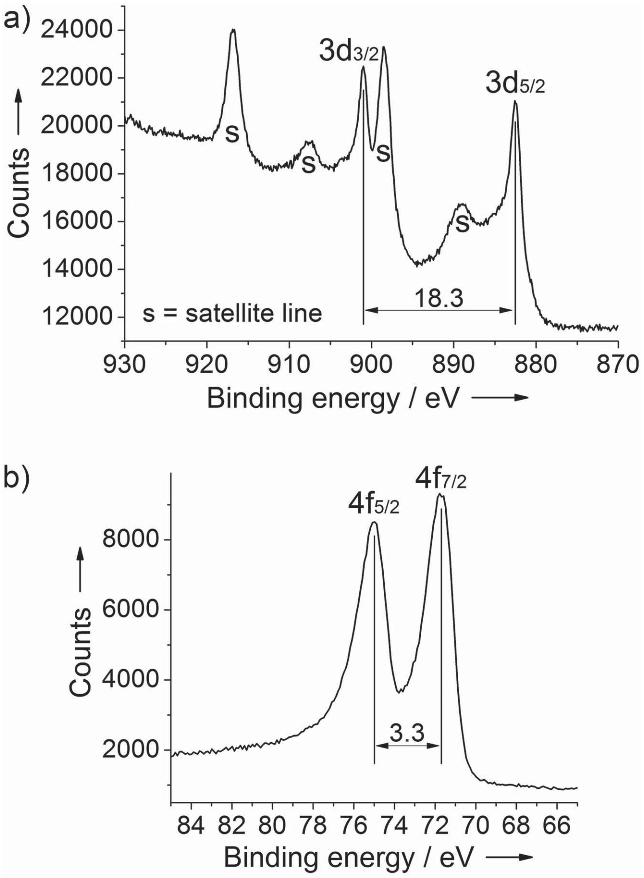

Figure 3. a) Ce 3d and b) Pt 4f XP spectra obtained from the Pt_a/CeO_2 that was prepared by photochemical reduction of H_2PtCl_6 in 1/1 (v/v) $EtOH/H_2O$ under UV irradiation without any additives.

CeO_2 nanofibers in the HAADF-STEM image (**Figure 5**a) due to the small size of Pt nanoparticles. These Pt nanoparticles were not only smaller and more uniform in size, but also distribute more uniformly across the entire surface of each porous CeO_2 nanofiber (Figure 5b). We did not observe Pt nanoparticles entrapped in the interparticle pockets of porous CeO_2 nanofibers as in Figure 4e. Figure 5c shows the typical distribution of Pt nanoparticles on the surface of CeO_2, in which all the Pt nanoparticles were well separated from each other. The interplanar spacings were 2.2 and 3.1 Å for the Pt nanoparticles and the underlying surface, which correspond to the (111) lattice planes of Pt and CeO_2, respectively (Figure 5d). The chemical compositions were further confirmed by selected area energy dispersive X-ray spectroscopy (EDS). As shown in Figure 5e, the nanoparticle (position 1) was comprised of pure Pt and the empty surface (position 2) was consisted of Ce and O. Figure 5f shows the high-resolution Pt 4f spectrum of Pt_c/CeO_2, which was essentially the same as that of Pt_a/CeO_2 (Figure 3b). The binding energies of Pt $4f_{5/2}$ and Pt $4f_{7/2}$ are 75.0 and 71.7 eV, respectively, which correspond to Pt(0).[4e] No shoulder peaks can be discerned in the spectrum, which confirms that Pt^{4+} species were fully reduced to Pt^0 nanoparticles through electronically excited reduction route.

We surveyed the diameters of a large number of Pt nanoparticles deposited on the surface of porous CeO_2 nanofibers prepared using the aforementioned three methods. The distributions are shown in **Figure 6**, in which more than 200 representative nanoparticles were measured. It is obvious that the average diameter of the Pt nanoparticles decreased after the addition of PVP and 4-benzyolbenzoic acid. In detail, Pt nanoparticles in Pt_a/CeO_2 had the largest average diameter of 16.7 nm. They also showed the broadest size distribution among the three samples, which varied from 8 to 28 nm (Figure 6a). The large size for the Pt nanoparticles in Pt_a/CeO_2 can be attributed to the agglomeration of small clusters during reduction (Figure 4b). The average particle size was dramatically reduced to 2.2 nm when PVP was introduced into the reaction solution and the size distribution of Pt nanoparticles in Pt_b/CeO_2 also fell into a narrower range of 1.0–4.0 nm (Figure 6b). Upon the addition of both PVP and 4-benzyolbenzoic acid, the average size of the resultant Pt nanoparticles further decreased to 1.7 nm and the distribution shifted to the range of 0.5–3.0 nm (Figure 6c). The size reduction and improvement in uniformity were direct results of the prevention of nanoparticle agglomeration as well as the increased reaction rate with the addition of a colloidal stabilizer and UV-sensitive molecules during photochemical reduction.

2.3. Catalytic Activity of Pt/CeO_2 toward the Water-Gas Shift Reaction

The porous CeO_2 nanofibers loaded with Pt nanoparticles (3% Pt loading) were evaluated as catalysts for the water-gas shift reaction. The catalytic activity of Pt/CeO_2 toward the water-gas shift reaction was measured in a fixed-bed reactor coupled with a gas chromatograph. **Figure 7**a shows the plots of CO conversion ratio as a function of temperature for pure CeO_2, Pt_a/CeO_2, Pt_b/CeO_2, and Pt_c/CeO_2. The feeding gas containing 2 vol% CO, 10 vol% H_2O, and 88 vol% helium was allowed to pass through the reactor at a total flow rate of 40 mL min^{-1}, corresponding to a weight hourly space velocity (WHSV) of 120 000 mL g_{cat}^{-1} h^{-1}. Due to the exothermic nature of the water-gas shift reaction, a low reaction temperature is desired. However, the reaction is extremely slow at low temperatures, leading to low conversion for CO. As such, it is important to choose an appropriate temperature range to achieve good catalytic conversion for CO. In the measurements, we chose to work in the temperature range from 350 to 450 °C and the CO conversion was obtained by analyzing the concentrations of CO and CO_2 in the effluent gas. The porous CeO_2 nanofibers without Pt loading were used as a blank control to determine the base line of CeO_2 and its CO conversion was only 0%–1% below 450 °C. As shown in Figure 7, the CO conversion increases with the increase of temperature. The Pt_c/CeO_2 was already active at 350 °C and its CO conversion was 46%. Whereas at the same temperature, the CO conversion of Pt_b/CeO_2 was 25% and the Pt_a/CeO_2 and pure CeO_2 showed no activity. As the temperature went up to 450 °C, the CO conversion reached 95% for the Pt_c/CeO_2, which is quite remarkable when compared with the literature values (40%–90% for 1–5 wt% Pt/CeO_2 at 400–500 °C and similar WHSV).[24] As a comparison, the CO conversion ratios over Pt_b/CeO_2, Pt_a/CeO_2, and pure CeO_2 at 450 °C were 53%, 5%, and 1%, respectively. The high activity of Pt_c/CeO_2 can be attributed to the smaller

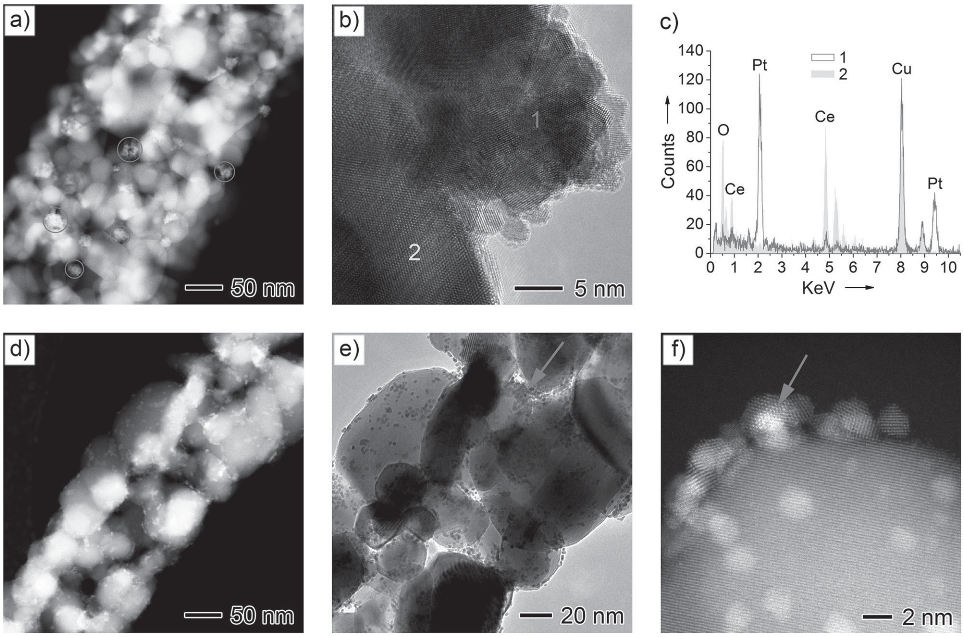

Figure 4. a) HAADF-STEM image showing Pt agglomerates (circled) that were deposited on the porous CeO_2 nanofibers (Pt_a/CeO_2) during photochemical reduction of H_2PtCl_6 in 1/1 (v/v) EtOH/H_2O under UV irradiation without any additives. b) HRTEM showing a Pt agglomerate and c) the corresponding EDS of selected areas (position 1 and 2). d) HAADF-STEM image showing Pt nanoparticles that were deposited on the porous CeO_2 nanofibers (Pt_b/CeO_2) in the presence of PVP. e) TEM and f) HAADF-STEM images showing the small aggregates of Pt nanoparticles (arrowed) on the surface of CeO_2 nanofibers in the presence of PVP only.

size of the Pt nanoparticles and their uniform distribution on the entire surface of each porous CeO_2 nanofiber.

The stability of a catalyst under the reaction conditions is another important indicator to evaluate its performance. Since Pt_a/CeO_2 was almost inactive below 450 °C, here we only compared the stability of Pt_b/CeO_2 and Pt_c/CeO_2. We conducted the gas-shift reaction at 400 °C over these two catalysts. At 400 °C, the CO conversion over the Pt_c/CeO_2 was around 71% with

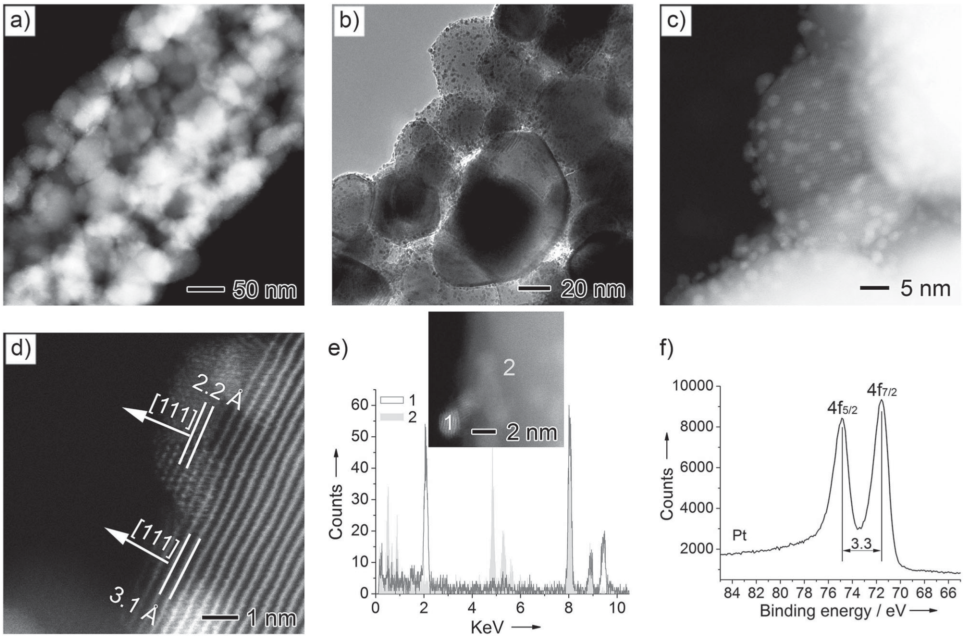

Figure 5. a–c) HAADF-STEM and TEM images at increasing magnifications showing uniform distribution of discrete Pt nanoparticles on porous CeO_2 nanofibers (Pt_c/CeO_2) by conducting the photoreduction in the presence of both PVP and 4-benzoylbenzoic acid. d) HAADF-STEM image showing the interface between Pt nanoparticles and CeO_2. e) EDS of selected areas. f) Pt 4f XP spectrum obtained from the Pt_c/CeO_2 that was prepared by reducing H_2PtCl_6 under UV irradiation in the presence of both PVP and 4-benzoylbenzoic acid.

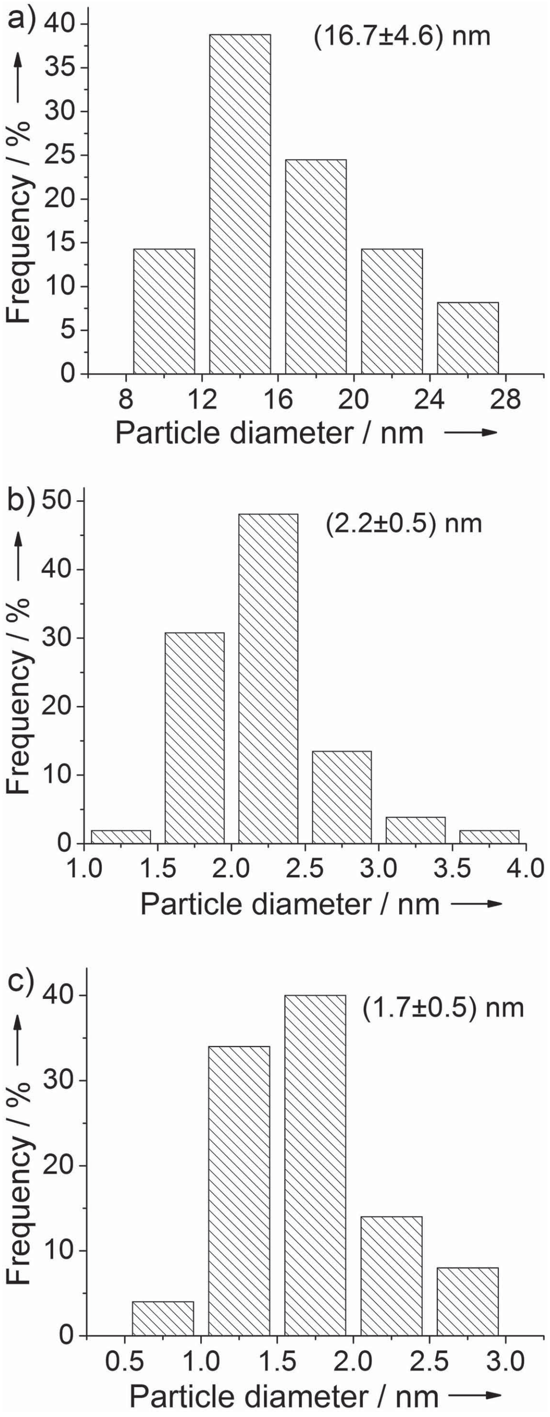

Figure 6. The diameter distributions of Pt nanoparticles deposited on the porous CeO_2 nanofibers under three different conditions: a) Pt_a/CeO_2, b) Pt_b/CeO_2, and c) Pt_c/CeO_2.

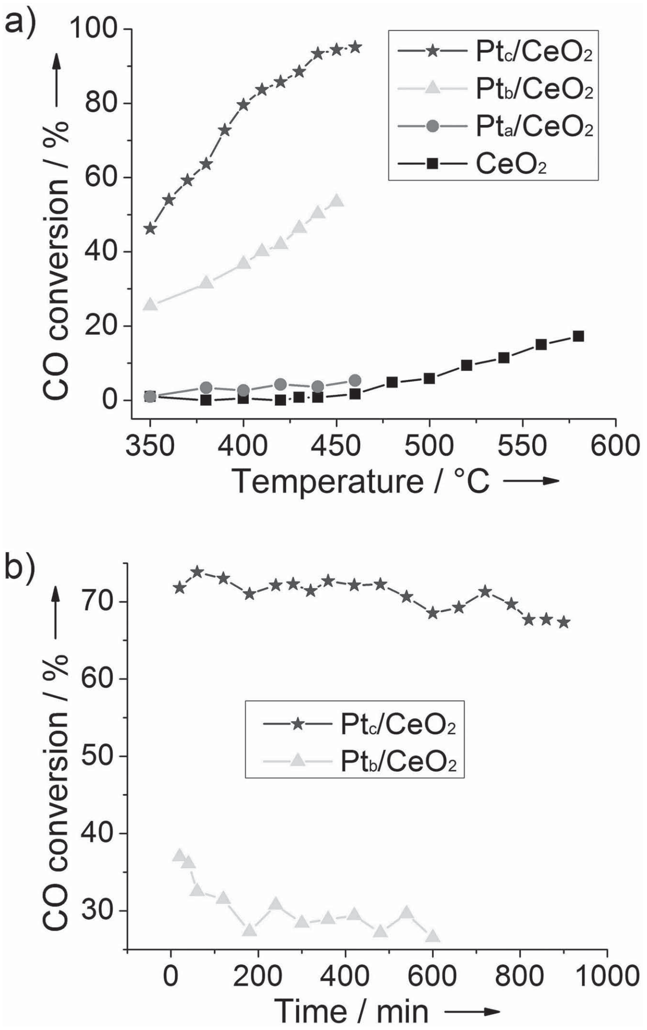

Figure 7. a) Temperature dependence of CO conversion for the water-gas shift reaction with the use of different catalysts. b) CO conversion as a function of time for the water-gas shift reaction with the use of two different catalysts. The subscripts a, b, and c are referred to the samples prepared through direct reduction without any additives, with the addition of PVP only, and with the introduction of both PVP and 4-benzyolbenzoic acid, respectively.

small fluctuations within the range of 73%–69% in 10 h. No deactivation occurred for the Pt_c/CeO_2 in the period of 10 h we tested at 400 °C. In contrast, the CO conversion decreased from 37% to 26% over the Pt_b/CeO_2 at 400 °C when reaction time was extended to 10 h, leading to the deactivation of catalyst. The deactivation is mainly caused by the migration and sintering of the Pt nanoparticles in Pt_b/CeO_2, which was confirmed by HRTEM observation. **Figure 8** shows the samples after stability test. The Pt nanoparticles in Pt_b/CeO_2 fused together to form large particles (Figure 8a), resulting in the decrease of specific surface area and thus catalytic activity. In comparison, the Pt nanoparticles in Pt_c/CeO_2 were still well distributed across the surface of each porous CeO_2 nanofiber without forming aggregates under the reaction conditions for 10 h at 400 °C (Figure 8b).

3. Conclusion

We have demonstrated a simple and reliable approach to the large-scale fabrication of porous CeO_2 nanofibers by electrospinning and calcination. The PAN matrix successfully prevented the collapse of fibrous structure during calcination

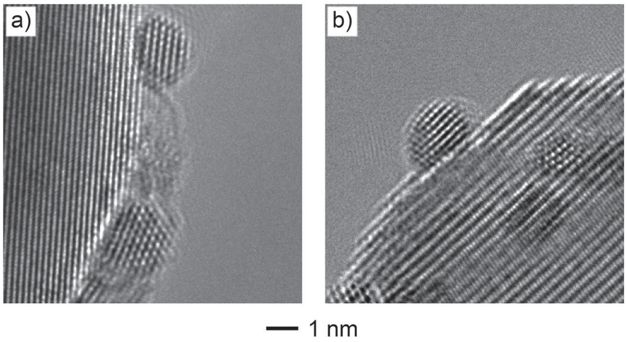

Figure 8. HRTEM images showing a) Pt_b/CeO_2 and b) Pt_c/CeO_2 after the stability test at 400 °C.

because of its physical stability under heating. Porous CeO_2 nanofibers were obtained after the complete removal of organic and carbon species by calcination in air at 800 °C. The hierarchically porous structure of CeO_2 nanofibers was characterized by SEM, TEM, HRTEM, HAADF-STEM, SAED, XRD, and XPS. The porous CeO_2 nanofibers were composed of interconnected nanoparticles with diameters in the range of 10–90 nm. The CeO_2 nanofibers were polycrystalline and are present in a face-centered fluorite cubic structure with an average crystallite size of about 40 nm. XPS confirmed that the Ce was completely oxidized during high-temperature calcination in air. The resultant porous CeO_2 nanofibers were then tested as a supporting material for Pt nanoparticles. We developed a photochemical method for the in situ formation and deposition of Pt nanoparticles on the porous CeO_2 nanofibers. In the presence of PVP and 4-benzyolbenzoic acid, Pt nanoparticles with an average diameter of 1.7 nm were generated under UV irradiation and evenly deposited on the entire surface of each porous CeO_2 nanofiber (Pt_c/CeO_2) with no aggregation. Without the addition of PVP and 4-benzyolbenzoic acid, large Pt agglomerates with an average diameter of 17 nm were produced (Pt_a/CeO_2). When only PVP was added, the Pt nanoparticles (2.2 nm) tended to form small aggregates in the interparticle pockets or pores (Pt_b/CeO_2). The Pt-loaded porous CeO_2 nanofibers were evaluated as catalysts for the water-gas shift reaction. The Pt_c/CeO_2 demonstrated the highest catalytic activity with 95% CO conversion at 450 °C while Pt_b/CeO_2, Pt_a/CeO_2, and pure CeO_2 only showed activities of 53%, 5%, and 1%, respectively. Moreover, a very stable catalyst for the water-gas shift reaction, the Pt_c/CeO_2 system showed a CO conversion of 71% at 400 °C for 10 h. The high activity and stability of Pt_c/CeO_2 for the water-gas shift reaction can be attributed to the smaller size of Pt nanoparticles and their uniform distribution on each porous CeO_2 nanofiber.

4. Experimental Section

Chemicals and Materials: Cerium(III) acetylacetonate hydrate, polyacrylonitrile (average $M_w \approx 150\,000$), 4-benzoylbenzoic acid (99%), hexachloroplatinic(IV) acid (H_2PtCl_6, 99.995%), and poly(vinyl pyrrolidone) ($M_w \approx 55\,000$) were all obtained from Sigma-Aldrich. Anhydrous *N,N*-dimethylformamide was purchased from EMD and ethanol (200 proof ACS grade) was received from VWR. All chemicals were used as received without further purification. Deionized water with a resistivity of 18.2 MΩ cm, purified using a Milli-Q plus system (Millipore), was used for all the experiments.

Fabrication of Porous CeO_2 Nanofibers: The porous nanofibers were prepared by coelectrospinning a DMF solution containing $Ce(acac)_3$) and PAN, followed by calcination in air to remove PAN and convert $Ce(acac)_3$ to CeO_2. Specifically, the $Ce(acac)_3$-PAN composite fibers were fabricated by electrospinning a DMF solution containing 5% $Ce(acac)_3$ and 10% PAN at 20 °C and under a relative humidity of 45%. In a typical process, the solution was loaded into a 3 mL syringe fitted with a 23 gauge flat metal needle of ≈2.5 cm long (BD Medical) and delivered at 1 mL h^{-1} using a syringe pump (KDS 200, KD Scientific). A voltage of 15 kV from a DC power source (ES 30-0.1 P, Gamma High Voltage Research) was applied to the vertically positioned needle. The charged jet was spun into fine fibers, which were collected on a rotating drum (1000 rpm) placed ≈15 cm below the tip of the needle. The as-prepared nonwoven mat of $Ce(acac)_3$-PAN fibers was dried in air for 1 d, followed by calcination at 800 °C in air for 2 h at a ramp rate of 10 °C min^{-1} to remove PAN and transform $Ce(acac)_3$ to CeO_2.

Photochemical Deposition of Pt Nanoparticles onto the Porous CeO_2 Nanofibers: The Pt nanoparticles were synthesized and deposited onto the porous CeO_2 nanofibers in situ using a photochemical method. Typically, 10 mg of the as-prepared CeO_2 nanofibers was added into 10 mL of ethanol/water ($EtOH/H_2O$, 1/1 v/v) mixture in a 20 mL glass vial (VWR), followed by sonication for 10 min to disperse the CeO_2 nanofibers. Subsequently, 1.65 mg of H_2PtCl_6 was introduced and dissolved by vortexing. This solution was degassed by bubbling with argon at 30 mL min^{-1} for 5 min. The vial was then sealed and placed side by side with an immersion well in a water bath. The light source was hosted inside the immersion well. The distance between the light source and the reaction solution was around 2 cm. Temperatures of both the water bath and the circulating water from the immersing well were kept at 20 ± 2 °C throughout the synthesis by controlling the flow rate of water. The UV irradiation in the range of 200–400 nm generated by a 500 W quartz mercury vapor arc lamp was allowed to continue for 3 h. The product was collected by centrifugation, washed three times with water to remove loosely bound Pt nanoparticles and residue reactants. This product was referred to as Pt_a/CeO_2. In the second experiment, 2.25 mg of PVP was mixed with the CeO_2 nanofibers. By using the same parameters and setup, we obtained the second product, which was referred to as Pt_b/CeO_2. By adding 10 mg of 4-benzyolbenzoic acid to the mixture of PVP and CeO_2 nanofibers, we produced the third product using the same procedure, which was referred to as Pt_c/CeO_2. These three products, namely, Pt_a/CeO_2, Pt_b/CeO_2, and Pt_c/CeO_2, were dried in vacuum at ambient temperature.

Catalytic Activity Measurement: The catalytic performance of Pt/CeO_2 for the water-gas shift reaction was carried out in a tubular fixed-bed reactor. In a typical measurement, 20 mg of the catalyst was diluted with SiO_2 to 80 mg. The feeding gas was composed of 2 vol% CO, 10 vol% H_2O, and 88 vol% helium. The gas flow rate was controlled at 40 mL min^{-1}, which resulted in a weight hourly space velocity (WHSV) of 120 000 mL g_{cat}^{-1} h^{-1}. The concentrations of CO and CO_2 in the effluent gas were analyzed using an online gas chromatograph (Agilent 7890A with HS-D 100/120 column and thermal conductivity detector, Agilent Technologies) with helium as the carrier gas.

Instrumentation: The surface morphology of the as-spun $Ce(acac)_3$-PAN nanofibers and the porous structure of the as-calcined CeO_2 nanofibers were examined using a SEM (Nova Nanolab 200 FIB/SEM, FEI) after Au coating for 60 s (Hummer). The images were taken at an accelerating voltage of 10 kV and a working distance of 5 mm. The diameters of the fibers and the particles were measured through the ImageJ software and then statistically analyzed using Origin 8 (OriginLab). TEM samples were prepared by placing a drop of the final product (suspended in water) on a carbon-coated copper grid and drying under ambient conditions. TEM images were taken using a JEOL 100CX microscope operated at 100 kV. HRTEM, HAADF-STEM imaging, and EDS analyses were performed using a field-emission JEOL ARM200F microscope with STEM Cs corrector operated at 200 kV. XPS was carried out using a Thermo K-Alpha XPS system with a monochromated Al Kα source (1486.7 eV). The X-ray spot size was 400 μm and mixed ion/electron charge compensation was used. Survey scans were recorded over an energy range of 0–1350 eV binding energy with a passing energy of 200 eV. High-resolution scans were taken for Ce and Pt with a passing energy of 50 eV, a step size of 0.01 eV, and a dwell time of 50 ms/step. Powder XRD patterns were measured on a Philips X'pert Pro Alpha-1 diffractometer equipped with an X'celerator module using Cu Kα radiation (λ = 1.5406 Å). Diffractograms were recorded from $2\theta = 20°$ to $80°$ with a step size of 0.02° and a scanning rate of 1 s/step at an operating voltage of 45 kV and a filament current of 40 mA. The samples for XPS and XRD measurements were prepared by adding concentrated CeO_2 and Pt/CeO_2 suspensions on silicon wafers and drying under vacuum. Inductively coupled plasma mass spectrometry (ICP-MS, NexION 300Q, Perkin-Elmer) was used to determine the Ce and Pt contents in the samples.

Supporting Information

Supporting Information is available from the Wiley Online Library or from the author.

Received: April 7, 2015
Revised: April 26, 2015

[1] a) C. Paun, O. V. Safonova, J. Szlachetko, P. M. Abdala, M. Nachtegaal, J. Sa, E. Kleymenov, A. Cervellino, F. Krumeich, J. A. van Bokhoven, *J. Phys. Chem. C* **2012**, *116*, 7312; b) Y. Lin, Z. Wu, J. Wen, K. R. Poeppelmeier, L. D. Marks, *Nano Lett.* **2014**, *14*, 191.
[2] a) K. B. Zhou, Z. Q. Yang, S. Yang, *Chem. Mater.* **2007**, *19*, 1215; b)I. I. Soykal, H. Sohn, D. Singh, J. T. Miller, U. S. Ozkan, *ACS Catal.* **2014**, *4*, 585.
[3] a) J.-M. Herrmann, C. Hoang-Van, L. Dibansa, R. Harivololona, *J. Catal.* **1996**, *159*, 361; b) J. F. d. Lima, R. F. Martins, C. R. Neri, O. A. Serra, *Appl. Surf. Sci.* **2009**, *255*, 9006; c) Z. Hu, H. Metiu, *J. Phys. Chem. C* **2012**, *116*, 6664; d) Y. Liu, Y. Ding, L. Zhang, P.-X. Gao, Y. Lei, *RSC Adv.* **2012**, *2*, 5193; e) J. Qi, J. Chen, G. D. Li, S. X. Li, Y. Gao, Z. Y. Tang, *Energy Environ. Sci.* **2012**, *5*, 8937; f) L. Adijanto, D. A. Bennett, C. Chen, A. S. Yu, M. Cargnello, P. Fornasiero, R. J. Gorte, J. M. Vohs, *Nano Lett.* **2013**, *13*, 2252; g) Z. Wang, X. Shao, X. Hu, G. Parkinson, K. Xie, D. Dong, C.-Z. Li, *Catal. Today* **2014**, *228*, 199; h) S. S. Rayalu, D. Jose, P. A. Mangrulkar, M. Joshi, G. Hippargi, K. Shrestha, K. Klabunde, *Int. J. Hydrogen Energy* **2014**, *39*, 3617; i) A. Tanaka, K. Hashimoto, H. Kominami, *J. Am. Chem. Soc.* **2012**, *134*, 14526; j) A. Tanaka, K. Hashimoto, H. Kominami, *ChemCatChem* **2011**, *3*, 1619.
[4] a) C. Q. Chen, Y. Yu, W. Li, C. Y. Cao, P. Li, Z. F. Dou, W. G. Song, *J. Mater. Chem.* **2011**, *21*, 12836; b) T. Tatte, M. Hussainov, M. Paalo, M. Part, R. Talviste, V. Kiisk, H. Mandar, K. Pohako, T. Pehk, K. Reivelt, M. Natali, J. Gurauskis, A. Lohmus, U. Maeorg, *Sci. Technol. Adv. Mater.* **2011**, *12*, 034412; c) S. S. Lee, H. G. Zhu, E. Q. Contreras, A. Prakash, H. L. Puppala, V. L. Colvin, *Chem. Mater.* **2012**, *24*, 424; d) E. Aneggi, D. Wiater, C. de Leitenburg, J. Llorca, A. Trovarelli, *ACS Catal.* **2013**, *4*, 172; e) Y. Gao, W. Wang, S. Chang, W. Huang, *ChemCatChem* **2013**, *5*, 3610; f) F. Gu, Z. Wang, D. Han, C. Shi, G. Guo, *Mater. Sci. Eng., B* **2007**, *139*, 62; g) Q. Cui, X. Dong, J. Wang, M. Li, *J. Rare Earths* **2008**, *26*, 664.
[5] Y. Xia, P. Yang, Y. Sun, Y. Wu, B. Mayers, B. Gates, Y. Yin, F. Kim, H. Yan, *Adv. Mater.* **2003**, *15*, 353.
[6] D. Li, Y. Xia, *Adv. Mater.* **2004**, *16*, 1151.
[7] X. G. Yang, C. L. Shao, Y. C. Liu, R. X. Mu, H. Y. Guan, *Thin Solid Films* **2005**, *478*, 228.
[8] G. C. Pontelli, R. P. Reolon, A. K. Alves, F. A. Berutti, C. P. Bergmann, *Appl. Catal. A* **2011**, *405*, 79.
[9] A. M. Azad, T. Matthews, J. Swary, *Mater. Sci. Eng. B* **2005**, *123*, 252.
[10] Y. Zhang, J. Li, Q. Li, L. Zhu, X. Liu, X. Zhong, J. Meng, X. Cao, *J. Colloid Interface Sci.* **2007**, *307*, 567.
[11] L. Xu, H. Song, B. Dong, Y. Wang, J. Chen, X. Bai, *Inorg. Chem.* **2010**, *49*, 10590.
[12] C. Li, R. Chen, X. Zhang, S. Shu, J. Xiong, Y. Zheng, W. Dong, *Mater. Lett.* **2011**, *65*, 1327.
[13] a) P. Lu, Q. Huang, A. Mukherjee, Y.-L. Hsieh, *ACS Appl. Mater. Interfaces* **2010**, *2*, 3738; b) S. W. Verbruggen, S. Deng, M. Kurttepeli, D. J. Cott, P. M. Vereecken, S. Bals, J. A. Martens, C. Detavernier, S. Lenaerts, *Appl. Catal. B* **2014**, *160*, 204; c) S. Deng, S. W. Verbruggen, Z. He, D. J. Cott, P. M. Vereecken, J. A. Martens, S. Bals, S. Lenaerts, C. Detavernier, *RSC Adv.* **2014**, *4*, 11648.
[14] a) T. Omata, S. Sasai, Y. Goto, M. Ueda, S. Otsuka-Yao-Matsuo, *J. Electrochem. Soc.* **2006**, *153*, A2269; b) M. F. García-Sánchez, A. Ortiz, G. Santana, M. Bizarro, J. Peña, F. Cruz-Gandarilla, M. A. Aguilar-Frutis, J. C. Alonso, *J. Am. Ceram. Soc.* **2010**, *93*, 155.
[15] a) Y. Q. Dai, B. Lim, Y. Yang, C. M. Cobley, W. Y. Li, E. C. Cho, B. Grayson, P. T. Fanson, C. T. Campbell, Y. M. Sun, Y. Xia, *Angew. Chem., Int. Ed.* **2010**, *49*, 8165; b) P. Lu, C. T. Campbell, Y. Xia, *Nano Lett.* **2013**, *13*, 4957.
[16] a) E. Formo, Z. Peng, E. Lee, X. Lu, H. Yang, Y. Xia, *J. Phys. Chem. C* **2008**, *112*, 9970; b) E. Formo, M. S. Yavuz, E. P. Lee, L. Lane, Y. Xia, *J. Mater. Chem.* **2009**, *19*, 3878; c) E. Formo, P. H. C. Camargo, B. Lim, M. Jiang, Y. Xia, *Chem. Phys. Lett.* **2009**, *476*, 56.
[17] a) Y. Ding, Y. Wang, L. Zhang, H. Zhang, C. M. Li, Y. Lei, *Nanoscale* **2011**, *3*, 1149; b) H. Tang, H. Sun, D. Chen, X. Jiao, *Mater. Lett.* **2012**, *77*, 7; c) Z. Zhang, Z. Wang, S.-W. Cao, C. Xue, *J. Phys. Chem. C* **2013**, *117*, 25939.
[18] K. Yoon, Y. Yang, P. Lu, D. Wan, H.-C. Peng, K. S. Masias, P. T. Fanson, C. T. Campbell, Y. Xia, *Angew. Chem. Int. Ed.* **2012**, *51*, 9543.
[19] T. Cao, Y. Li, C. Wang, L. Wei, C. Shao, Y. Liu, *J. Sol-Gel Sci. Technol.* **2010**, *55*, 105.
[20] A. R. Hwang, J. Park, Y. C. Kang, *Bull. Korean Chem. Soc.* **2011**, *32*, 3338.
[21] H. Einaga, M. Harada, *Langmuir* **2005**, *21*, 2578.
[22] A. Peled, M. Naddaka, J. P. Lellouche, *J. Mater. Chem.* **2012**, *22*, 7580.
[23] J. C. Scaiano, K. G. Stamplecoskie, G. L. Hallett-Tapley, *Chem. Commun.* **2012**, *48*, 4798.
[24] a) C. M. Y. Yeung, K. M. K. Yu, Q. J. Fu, D. Thompsett, M. I. Petch, S. C. Tsang, *J. Am. Chem. Soc.* **2005**, *127*, 18010; b) P. Piermartini, T. Schuhmann, P. Pfeifer, G. Schaub, *Top. Catal.* **2011**, *54*, 967; c) M. C. Ribeiro, G. Jacobs, L. Linganiso, K. G. Azzam, U. M. Graham, B. H. Davis, *ACS Catal.* **2011**, *1*, 1375; d) B. Liu, A. Goldbach, H. Xu, *Catal. Today* **2011**, *171*, 304; e) C. I. Vignatti, M. S. Avila, C. R. Apesteguía, T. F. Garetto, *Catal. Today* **2011**, *171*, 297; f) B. Liu, H. Xu, Z. Zhang, *Catal. Commun.* **2012**, *26*, 159.